



Microstructure and catalytic properties of Fe₃O₄/BN, Fe₃O₄(Pt)/BN, and FePt/BN heterogeneous nanomaterials in CO₂ hydrogenation reaction: Experimental and theoretical insights

Anton S. Konopatsky^{a,*}, Konstantin L. Firestein^b, Nikolai D. Evdokimenko^{a,c}, Alexander L. Kustov^{a,c,d}, Viktor S. Baidyshev^e, Il'ya V. Chepkasov^f, Zahar I. Popov^{a,g}, Andrei T. Matveev^a, Igor V. Shetinin^a, Denis V. Leybo^a, Ilia N. Volkov^a, Andrey M. Kovalskii^a, Dmitri Golberg^b, Dmitriy V. Shtansky^a

^a National University of Science and Technology "MISIS", Leninsky prospect 4, Moscow 119049, Russian Federation

^b Centre for Materials Science and School of Chemistry and Physics, Queensland University of Technology (QLD), 2 George st., Brisbane, QLD 4000, Australia

^c N.D. Zelinsky Institute of Organic Chemistry N.D. Zelinsky RAS, 47, Leninsky Prospekt, Moscow 119991, Russian Federation

^d Lomonosov Moscow State University, GSP-1, Leninskie Gory, Moscow 119991, Russian Federation

^e Katanov Khakas State University, 90 Lenin pr., 655017 Abakan, Russian Federation

^f Skolkovo Institute of Science and Technology 30, bld. 1 Bolshoy Boulevard, Moscow 121205, Russian Federation

^g Emanuel Institute of Biochemical Physics RAS, Kosygina 4, Moscow 119334, Russian Federation

ARTICLE INFO

Article history:

Received 6 June 2021

Revised 9 August 2021

Accepted 9 August 2021

Available online 23 August 2021

Keywords:

Heterogeneous catalysts

Hexagonal BN support

Fe₃O₄

FePt nanoparticles

Carbon dioxide hydrogenation

Molecular dynamic simulations

ABSTRACT

Hexagonal boron nitride (*h*-BN) nanosheets are a promising material for various applications including catalysis. Herein, *h*-BN-supported Fe-based catalysts are characterised with respect to CO₂ hydrogenation reaction. Heterogeneous Fe₃O₄/BN, Fe₃O₄(Pt)/BN, and FePt/BN nanostructures are obtained *via* polyol synthesis in ethylene glycol. The sizes of Fe₃O₄ nanoparticles and their distributions over *h*-BN surfaces depend on the amount of H₂PtCl₆ added to the synthesis media. Bimetallic FePt nanoparticles are formed when Pt content is high enough. *In situ* TEM analysis shows the formation of core-shell *h*-BN@FePt nanoparticles during heating that prevents FePt NPs from further sintering during the catalytic process. The mechanism of Fe and Pt interaction is elucidated based on the molecular dynamic simulations. The FePt/BN nanomaterials show significantly higher CO₂ conversion rate compared to the Fe₃O₄/BN and Fe₃O₄(Pt)/BN heterogeneous nanomaterials and exhibit almost 100% selectivity to carbon monoxide. The Fe₃O₄/BN and Fe₃O₄(Pt)/BN nanomaterials show better selectivity to hydrocarbons. The possible reaction pathways are discussed based on the calculated sorption energies of all reactants, intermediate compounds, and reaction products. The study highlights pronounced catalytic properties of the developed system and reveals a unique interaction mechanism between its components increasing their stability.

© 2021 Elsevier Inc. All rights reserved.

1. Introduction

Global climate change, greenhouse effect and uncontrolled temperature rise are among the most urgent problems nowadays [1–3]. Associated rising CO₂ emission due to human activity requires the development of effective ways to reduce its harmful impact [4–7].

Search and development of new materials for CO₂ utilization are in high demand [8]. Advanced catalytic materials are presumed to not only reduce CO₂ emission [9], but also to be used for produc-

tion of valuable hydrocarbons [10]. With such approach in mind, carbon dioxide is considered as a renewable source of energy [11–14].

Efficient implementation of CO₂ hydrogenation process requires the development of new advanced heterogeneous catalysts. This includes the selection of catalytically active nanoparticles (NPs) and appropriate support materials [15]. These substrates should have a combination of high specific surface area, chemical and thermal stability, and excellent mechanical properties. One of the promising carrier materials of catalytically active NPs is a hexagonal boron nitride (*h*-BN). It has high chemical stability, superb oxidation resistance (up to 900 °C), enhanced thermal stability (up to 1000 °C), and high tensile strength (~60 GPa) [16–19]. A number of theoretical works dedicated to *h*-BN-based catalysts has predicted

* Corresponding author.

E-mail address: konopatskiy@mis.ru (A.S. Konopatsky).

their high catalytic activity due to boron vacancies that contribute to the attachment of metal atoms to *h*-BN surfaces [20–22].

The interaction of catalytically active NPs and substrate materials significantly affects the catalytic properties [23–25]. For the specific NPs/substrate system the interface plays an important role in a catalytic process [26]. For example, in a Cu/ZrO₂ system, oxygen vacancies within the substrate facilitate incorporation of Cu atoms, which contribute to the increased catalytic activity of the material in methanol production during CO₂ hydrogenation process [27]. Higher adhesion energy of Ag to boron oxide, as compared to pristine *h*-BN surface, can be successfully exploited in order to control Ag nanoparticles content over *h*-BN surfaces [28]. A carrier and catalytically active NPs interaction can lead to new phases formation. Such phases can act as active sites in a catalytic reaction. For example, intermediate Fe₅C₂ phases have served as active sites in potassium-promoted Fe NPs deposited onto the surfaces of nanostructured graphene. Surface defects can also reduce the average size of Fe NPs and increase the activity and selectivity of a material [29].

Generally, iron, as catalytically active NPs, has a high potential for CO₂ hydrogenation [30]. Fe-based catalysts can be used for production of various hydrocarbons [31,32]. In order to increase the efficiency of Fe-based catalysts, various substrates and promoters have recently been utilized [33]. One of the main problems, when using Fe-based NPs, is their strong tendency to agglomeration. Therefore, their stabilization on a substrate for prevention of catalyst deactivation is an important scientific task. Introduction of Mn, as a promoter, during Fe-based NP synthesis has led to the formation of core-shell NPs with increased stability over a silica substrate [34]. Sodium carboxymethyl cellulose has been used for bimetallic Fe-Pd NP stabilization in catalytic reduction process of *para*-nitrochlorobenzene. Besides enhanced stability, such composite materials demonstrate higher chemical reactivity [35]. Precipitation of Fe-based NPs onto the surfaces with specifically designed topography is also considered as a stabilization method. It has been demonstrated that Fe-based NPs are successfully trapped within mesoporous silica [36]. In Ref. [37] it has been demonstrated that iron additions into biochar enhances CO₂ sorption due to the chemical reaction between CO₂ and Fe.

Herein, we study the effects of *h*-BN carriers on the structure and properties of Fe(Pt)/BN heterogeneous nanocatalysts. The main research goal is to elucidate interrelations between the chemical/phase composition, structure, and properties of the developed materials. Catalytic performance of the Fe(Pt)/BN systems in a reaction of CO₂ hydrogenation is under spotlight. Special attention is paid to studying the effect of *h*-BN substrate on the agglomeration process of catalytically active Fe-based NPs at elevated temperatures.

2. Experimental

2.1. Samples preparation

Fe(Pt)/BN nanomaterials were synthesized using a polyol process. The used protocol was based on the synthesis scheme described elsewhere [38]. 100 ml of ethylene glycol (EG) was used as a synthesis media. *h*-BN powder with an average particle size of 50 nm was dispersed in EG using a magnetic stirrer and an ultrasound homogenizer (hd2200, «Bandelin»). In order to prevent *h*-BN agglomeration, the obtained mixture was placed in a holder and subjected to continuous mild sonication. H₂PtCl₆ solution was used as a Pt source. Certain amount of acid was added into the mixture. The system was heated up to 165 °C and then 600 mg of FeCl₂·4(H₂O) and 5 g of NaOH were added. When synthesis had been completed (approximately after 2 min), the system

was cooled down to room temperature. In order to obtain heterogeneous nanomaterials, centrifugation procedure was implemented using a Universal 320 centrifuge (HETTICH). Precipitates obtained after 3rd rinsing were dried overnight. The same protocol was implemented in order to obtain unsupported Fe(Pt) NPs used as reference samples. The sample description is given in Table 1.

2.2. Structural analysis

A field emission JEOL 7600F scanning electron microscope equipped with an energy dispersive X-ray spectroscopy (EDX) detector was used for investigation of nanocatalyst morphology and its chemical composition. EDX analysis was conducted on a large area of each sample (>100 μm²).

Microstructure analysis, including that during *in situ* heating, was performed using a JEM-2100 transmission electron microscope (JEOL) operated at 200 kV. Phase composition was investigated by means of X-ray diffraction (XRD) using a Shimadzu diffractometer (Cu-Kα radiation (λ = 1.54178 Å)). X-ray photoelectron spectroscopy (XPS) was conducted using an Axis Supra unit (Kratos Analytical). For the energy scale calibration, C1s peak was fixed at 285.0 eV. CasaXPS software and Shirley approximation were used for a fitting procedure and background correction, respectively. Fourier-transform infrared spectroscopy (FTIR) was conducted using a Vertex 70v equipment (Bruker). For the thermogravimetric analysis (TGA), a STA 449 F3 Jupiter equipment (Netzsch) was utilized. The sample mass for TGA was 15 mg. Surface characterization was conducted by BET and BJH techniques (Quantachrome Instruments) using N₂ gas.

2.3. Carbon dioxide hydrogenation reaction

A fixed-bed continuous-flow reactor was used for catalytic tests on the obtained heterogeneous nanomaterials. The height of the catalyst layer was about 3 diameters of the reactor which allowed us to achieve a uniform flow at the same rate throughout the whole volume of the catalyst. For catalytic activity and selectivity tests, 100 mg of each sample were used. Reaction kinetics was studied using 5 mg samples. Catalytic tests were carried out at 20 atm and a space velocity of 500 h⁻¹ to study the activity and selectivity of the samples and 400,000 h⁻¹ to study the reaction kinetics. The H₂:CO₂ ratio in the initial mixture was 2:1. The products were analyzed on-line using a Crystal 5000 gas chromatograph equipped with three thermal conductivity detectors, a flame ionization detector, packed columns M ss316 NaX 80/100 mesh 2 m × 2 mm, HayeSep R 80/100 mesh 1 m × 2 mm, HayeSep Q 80/100 mesh 1 m × 2 mm and a capillary column MXT®-Alumina BOND/MAPD 30 m × 0.53 mm. The mass balance of the reaction products, calculated by the method of absolute calibration, was reduced in carbon and amounted at ≥ 98%. The following activation scheme was implemented for all studied materials: 500 °C over 8 h in a stream of hydrogen. Activation was carried out in the catalytic reactor prior to each test. Turnover frequency

Table 1
Sample description.

Sample	Initial Fe/Pt molar ratio	Description
FO/BN	n/a	Heterogeneous nanostructures Fe ₃ O ₄ /BN
FO		Unsupported NPs Fe ₃ O ₄
FO(Pt)/BN	120,000	Heterogeneous nanostructures Fe ₃ O ₄ (Pt)/BN
FO(P)		Unsupported NPs Fe ₃ O ₄ (Pt)
FP/BN	60	Heterogeneous nanostructures FePt/BN
FP		Unsupported NPs FePt

(TOF) values were calculated as the ratio of the reaction rate and specific surface area of the catalyst measured as the number of the adsorbed N_2 molecules derived from the BET analysis.

2.4. Modeling

The simulations were carried out using the molecular dynamics (MD) methods in LAMMPS program package [39]. The analytical bond-order potential (ABOP) [40,41] was applied in all MD simulations (Fig. S1 and S2). All quantum-chemical calculations were performed within the framework of density functional theory (DFT) [42,43] implemented in a VASP program package [44–46]. The revised Perdew, Burke, and Ernzerhof (rPBE) exchange–correlation functional was used [47]. The projector-augmented wave (PAW) method based on pseudopotentials was applied in plane wave basis with the energy cutoff of 400 eV.

3. Results and discussion

3.1. Material structure

The characteristic microstructures of Fe(Pt)/BN catalysts and the results of their chemical EDS analyses are shown in Fig. 1. Small spherical NPs densely populate the surfaces of numerous curved *h*-BN nanosheets (Fig. 1a–c). A FO/BN composite contains a noticeably greater amount of larger NPs (up to 70 nm) as compared to other samples. Comparison of the TEM images taken from FO/BN

and FO(P)/BN samples and their corresponding EDX spectra suggest that the higher Fe concentration in the FO/BN is due to the formation of larger NPs. NPs in the FP/BN sample demonstrate a sharper contrast due to supposedly higher average atomic (*Z*) number of the constituting phase. Appearance of noticeable Pt signal in the corresponding EDX spectrum (Fig. 1i) allows us to suggest that bimetallic FePt NPs were formed on the surfaces of *h*-BN.

The high-resolution TEM images of individual NPs and corresponding Fast Fourier Transform (FFT) patterns are presented in Fig. 1d–f. The following interplanar distances were indicated for the FO/BN sample: 0.333 nm, 0.291 nm, 0.251 nm, and 0.205 nm, which can be attributed to the (002) *h*-BN (0.334 nm), (220) Fe_3O_4 (0.297 nm), (311) Fe_3O_4 (0.253 nm), and (400) Fe_3O_4 (0.209 nm) planes [48]. The same phases were identified in the FO(P)/BN sample: characteristic interplanar distances of 0.337 nm, 0.292 nm, 0.257 nm, and 0.214 nm belong to (002) *h*-BN (0.334 nm), (220) Fe_3O_4 (0.297 nm), (311) Fe_3O_4 (0.253 nm), and (100) *h*-BN (0.217 nm) planes. Thus, the FO/BN and FO(P)/BN samples are mainly represented by heterogeneous *h*-BN and Fe_3O_4 nanostructures. Different phase composition was observed in the FP/BN sample. According to Fig. 1f (inset), the interplanar distances are: 0.336 nm, 0.224 nm, 0.194 nm and 0.216 nm, which correspond well to (002) *h*-BN (0.334 nm), (111) *fcc* FePt (0.228 nm), (200) *fcc* FePt (0.197 nm) and (100) *h*-BN (0.217 nm) planes [49]. The obtained results demonstrate that the FP/BN sample mainly consists of *h*-BN and bimetallic FePt NPs.

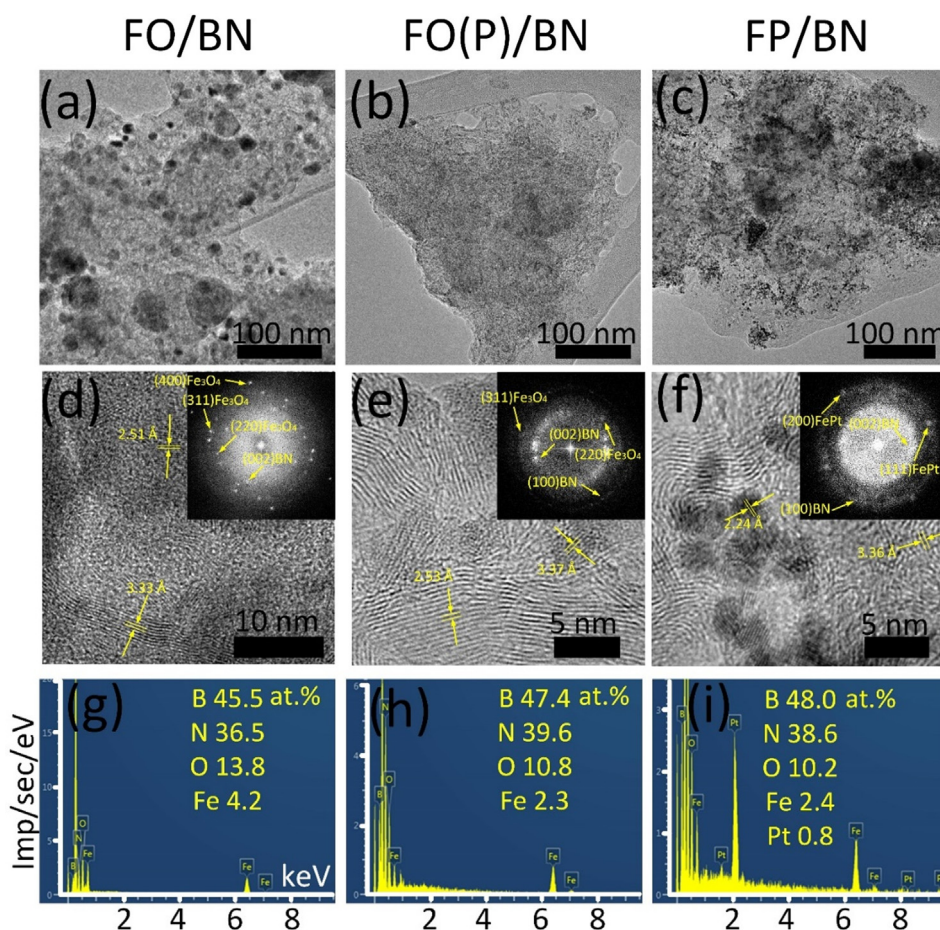


Fig. 1. Microstructure and elemental composition of FO/BN, FO(P)/BN, and FP/BN samples: (a)–(c) TEM images, (d)–(f) HRTEM images with corresponding FFT patterns depicted in the insets, (g)–(i) EDX spectra.

Scanning TEM (STEM) images of the FP/BN, FO(P)/BN, and FO/BN nanomaterials with corresponding EDS elemental maps and XRD spectra are depicted in Fig. 2. All metallic elements are homogeneously distributed over the *h*-BN surfaces. Note that Fe and Pt distributions are similar, further proving formation of bimetallic FePt NPs (Fig. 2c). XRD patterns of the FO/BN and FO(P)/BN samples indicate that the *h*-BN and Fe₃O₄ are the main phases, although a small amount of pure Fe (in the form of a few large Fe NPs (>50 nm)) is also present [50]. When a small amount of Pt had been added into the synthesis media, the Fe₃O₄ peak became wider and less intensive. This indicates that large Fe₃O₄ NPs are not present in the FO(P)/BN sample. It can be suggested that even a small concentration of Pt in the synthesis media provides more nucleation centers leading to the smaller sizes of Fe₃O₄ precipitates. The main peaks in the XRD pattern of FP/BN nanocomposite were from the *h*-BN and FePt phases (Fig. 2f) [51–53], although low intensity peaks of Fe₃O₄ phase were also visible. This means that in the presence of Pt the bimetallic NP formation dominates over Fe oxidation. XRD patterns of selected support-free and *h*-BN-supported NPs are presented in Fig. 2. The crystallite size calculated using the Scherer formula is 10.8 (FO), 8.1 (FO/BN), 6.8 (FO(P)), 5.2 (FO(P)/BN), 7.6 (FP), and 2.9 nm (FP/BN). In all cases, the size of Fe-based NPs supported by *h*-BN is smaller. In addition, as follows from Fig. 2g,i, after activation at 500 °C for 8 h, the particle size increased to 5.2 (FP/BN) and 12.5 nm (FP). This indicates that the *h*-BN support stabilizes the particles. Note that the bimetallic FePt NPs in the FP/BN sample are retained after activation and subsequent exposure to air, while the Fe₃O₄ phase is completely reduced to Fe. In the case of support-free FP NPs, the Fe₃O₄, Fe₂O₃, Fe and FePt phases are observed after activation.

3.2. Surface chemical state

XPS spectra of the obtained heterogeneous catalysts and reference samples (metal and oxide phases without carriers) are presented in Fig. 3 and Fig. S3, respectively. The B1s and N1s spectra are fitted using two components, namely BN and NBO. The BN phase is the main component with corresponding XPS B1s and N1s peaks located at 190.5 eV (FO/BN), 190.7 eV (FO(P)/BN) and 190.8 eV (FP/BN), and at 397.8 eV (FO/BN), 398.3 eV (FO(P)/BN), 398.4 eV (FP/BN), respectively. The content of NBO phase increases from approximately 25% (FO/BN) to 30% (FO(P)/BN and FP/BN samples). This leads to a slight shift of B1s and N1s peaks toward the higher BE values. The higher content of BNO phase in the FP/BN and FO(P)/BN samples compared to the FO/BN counterpart can be explained by a large number of small oxidized NPs forming O–BN bonds with the BN support [54].

The Fe3p peaks in the XPS spectra of FO/BN, FO(P)/BN and FP/BN samples are located at 56.5, 56.2, and 56.4 eV, respectively. In the FO/BN and FO(P)/BN nanohybrids, the Fe3p peaks are fitted using the Fe²⁺ and Fe³⁺ components. This indicates that the Fe NPs are mostly oxidized; this is in agreement with the XRD data showing that the Fe₃O₄ phase is the main component. Although the Fe₍₁₀₀₎ peak is visible in the XRD patterns of FO/BN and FO(P)/BN samples, the Fe⁰ component is not observed in the XPS spectra due to the surface oxidation of larger Fe NPs. The presence of stoichiometric Fe₃O₄ oxide is evidenced by the Fe²⁺:Fe³⁺ ratio close to 1:2 [57,58]. In the FP/BN sample, an additional component at 53.0 eV is observed, which can be attributed to the Fe⁰. Low intensity of the Fe⁰ peak and the simultaneous presence of Fe²⁺ and Fe³⁺ components suggest surface oxidation of bimetallic NPs [55,56]. For the Pt-containing sample, two distinct Pt4f 5/2 and

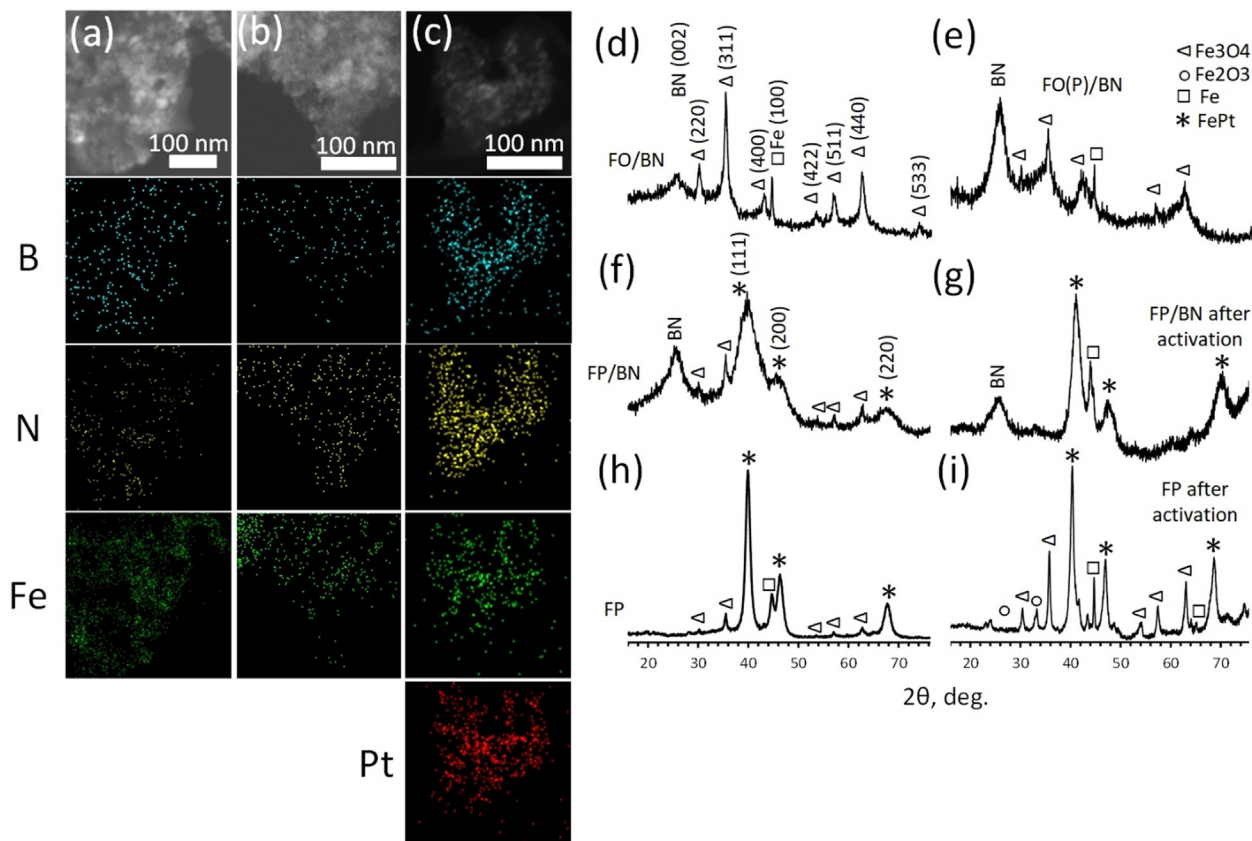


Fig. 2. STEM images (a, b, c) with corresponding spatially-resolved EDX elemental maps and XRD patterns (d–i) of FO/BN, FO(P)/BN, FP/BN, and FP samples before (d–f, h) and after (g, i) activation.

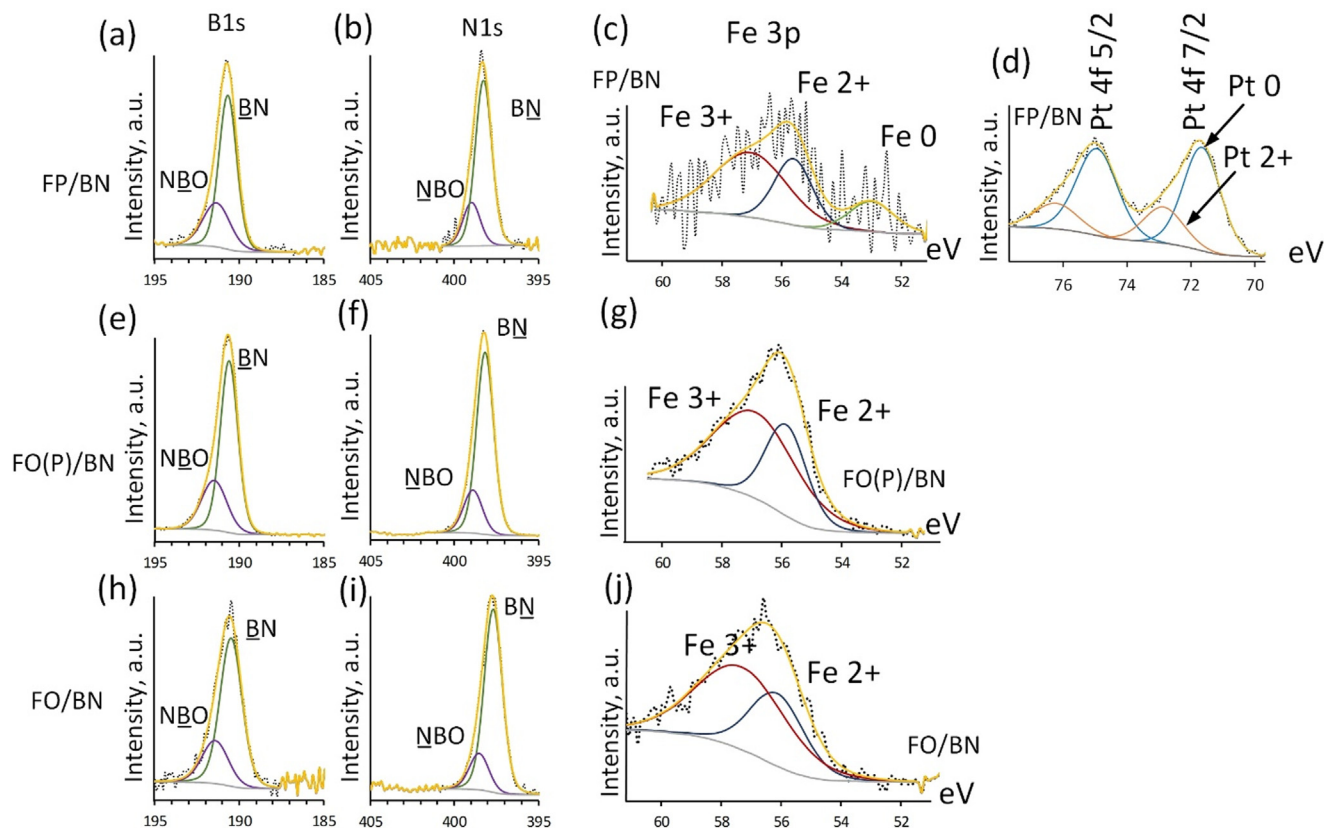


Fig. 3. XPS B1s (a, e, h), N1s (b, f, i), Fe3p (c, g, j), and Pt4f (d) spectra of FP/BN, FO(P)/BN, and FP/BN samples.

Pt4f 7/2 peaks at 74.9 and 71.6 separated by 3.3 eV can be seen, which is typical for metallic Pt (Fig. 3j, k). An additional, low-intensity component is attributed to the oxidized Pt^{2+} state [59]. Note that the signal-to-noise ratio of the Pt4f peaks is much higher than that for the Fe3p counterparts, which suggests that the surface of FePt NPs is enriched in Pt. Surface enrichment with Pt was also reported for bimetallic CoPt nanoparticles [60].

3.3. Thermogravimetric analysis

To identify the processes that may occur during activation stage, additional thermogravimetric experiments simulating activation conditions were carried out. Since in the Fe(Pt)/BN heterostructures the amount of catalytically active component was relatively low, we used the simplified model with pure catalytic phases. Additionally, FTIR analysis was conducted for all obtained samples. The results are given in Fig. 4.

Heating of the FP, FO(P) and FO materials in a hydrogen atmosphere leads to a considerable mass loss (Fig. 4a,b). Initial stage of mass loss is common for all samples. It starts from the very beginning of tests up to 200–220 °C. This stage is associated with a moisture and residual polymer desorption. Next stage occurring in the range of 220–350 °C can be ascribed to the reduction of Fe_3O_4 . This stage is absent in the case of FP sample due to bimetallic nature of the material. Indeed, according to the FTIR spectra (Fig. 4d), a pronounced signal from the Fe–O bonding was only observed for the Pt-free and FO(P) samples regardless of the h-BN presence. The iron oxides reduction by hydrogen depends on several factors: (i) processing conditions (temperature, heating rate etc.), (ii) reaction pathway [61], and (iii) oxide particles size. The rate of oxide reduction was shown to increase with decreasing Fe_3O_4 size [62,63]. Thus, the reduction processes can be more

intense when using smaller NPs, which is observed in the case of FO(P) material (Fig. 4b).

Generally, the Fe_3O_4 reduction by hydrogen at low temperatures (<390 °C) leads to the formation of metallic iron. At a higher temperature the FeO phase forms [64–66]. So, the second stage of mass loss in the FO(P) sample can be ascribed to the metallic Fe formation. This process is dominating since the third stage of mass loss is nearly indistinguishable. The same process takes place in the FO sample, but the FeO formation is more pronounced as reflected in the third stage of mass loss at a higher temperature (350–450 °C in Fig. 4c).

After TG analysis at 500 °C for 8 h, a mass loss plateau is observed approximately after 55 (FO(P)) and 100 min (FO), indicating complete reduction of all oxide phases. When testing the FP sample, a gradual increase in mass is observed over 400 min. This may be due to the hydrogenation of FePt NPs. Under test conditions, molecular hydrogen can dissociate onto the FePt surface and then adsorb in the atomic state.

3.4. Catalytic tests

Results of the catalytic tests (reaction rates, conversion percentage, and selectivity) are depicted in Fig. 5. The highest reaction rate is observed for the FP/BN sample with $918.64 \text{ CO}_2 \text{ mole/kg}_{\text{cat}} \times \text{h}$ (Fig. 5a). For other samples, the reaction rate was lower: 246.72 (FO(P)), 160.29 (FP), 152.88 (FO), 110.2 (FO(P)/BN), and $64.47 \text{ mol/kg}_{\text{cat}} \times \text{h}$ (FO/BN). These results allow us to elucidate the role of h-BN carriers in a CO_2 hydrogenation process. The specific surface area and the amount of catalytically active component are often considered as the main factors responsible for enhanced material catalytic performance. While the FO/BN and FO(P)/BN samples demonstrate the lower reaction rates compared to their

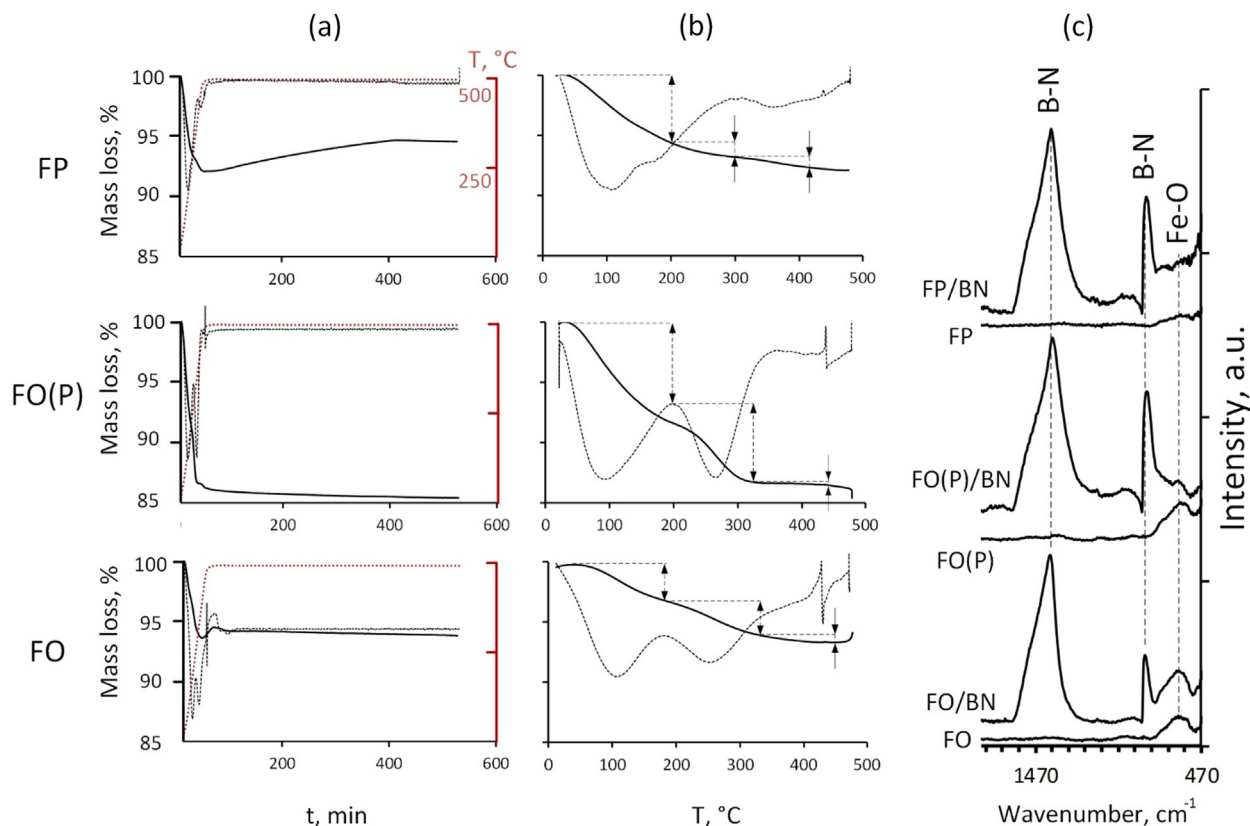


Fig. 4. TG and DTG curves for FP, FO(P) and FO samples obtained during (a) 8 h and the first 50 min of testing (b); (d) FTIR spectra.

BN-free counterparts in absolute value, they should be considered as more efficient once the difference in the amount of catalytically active component between these samples is taken into account. Note that the sintering process of freestanding NPs is more intense compared with those located on a support surface leading to a fast decrease in their specific surface area. In contrast, *h*-BN effectively anchors Fe oxide NPs over its surfaces preventing sintering and ensuring enhanced reaction kinetics.

More significant difference in the catalytic activity is observed for the FP and FP/BN samples. The FP/BN nanocomposite with bimetallic NPs demonstrates a five times higher reaction rate as compared to the BN-free counterpart. This can be explained by sintering of the FePt NPs above 500 °C, which is a well-known problem. In contrast, the *h*-BN with a specific morphology (thin curved nanosheets) significantly decreases tendency of the FePt NPs toward agglomeration at elevated temperature. The mechanism behind this effect is discussed below. As for catalytic activity, *i.e.* CO₂ conversion, the FP/BN catalyst demonstrates high, *i.e.* 25%,-conversion at 345 °C outperforming FO(P)/BN (2.4%) and FO/BN (1.9%) materials (Fig. 5b).

When comparing the FO/BN and FO(P)/BN samples, the latter shows a higher catalytic activity. This can be explained by a more complete reduction process of smaller iron oxide NPs during activation stage, which has been demonstrated during TGA analysis. Indeed, the more electrons are available on a 3d orbital, the more effectively adsorbed hydrogen can be activated. In terms of catalytic activity, iron oxides with a higher Fe oxidation state are affected by a slower redox mechanism [67–69]. The increased catalytic activity and almost 100% CO selectivity are apparently common for Pt-based bimetallic NPs and are associated with a change in the energy of d-band centers towards the lower values [70].

Since the studied materials have a different structure, and phase, and chemical compositions, for a more appropriate compar-

ison of their catalytic characteristics, turnover frequency (TOF) was determined for each specific surface area. The obtained results are collected in Table 2.

Based on the TOF values as a measure of the intrinsic material catalytic activity, it can be concluded that the FP/BN nanohybrid has an order of magnitude higher catalytic activity compared to two other tested samples. Note that the FO(P)/BN sample has a higher TOF (1.47 times) and reaction rate (1.72 times) compared to the FO/BN nanohybrid. To explain the difference, it can be assumed that the FO(P)/BN nanocomposite has more nanoparticles *per unit area* providing a larger number of active sites. Differences in the pore sizes and their volume for the studied materials have been analyzed by BJH method and are represented in Table S1. We also calculated the specific surface area of catalytically active nanoparticles using the corresponding TEM images. The obtained results are (m²/g_{cat}): FO/BN – 20.3, FO(P)/BN – 12.2, FP/BN – 13.2. This indicates that the absolute TOF values may be of almost an order of magnitude higher. However, the relative difference between the FO/BN, FO(P)/BN, and FP/BN samples in terms of their catalytic efficiency is almost independent of the specific surface area estimation method.

Regarding selectivity to hydrocarbons, the samples performed differently (Fig. 5c–e). The FP/BN nanocomposite shows almost 100% CO selectivity (Fig. 5c). However, the FO(P)/BN and FO/BN catalysts appear to be more efficient materials in terms of hydrocarbon production, despite lower conversion and reaction rates (Fig. 5d). Methane is the second reaction product after CO (Fig. 5e), and some C₂/C₃ species are also generated. The formation of CH is a much slower process than CO, which is the first stage in the CO₂ hydrogenation. The available data indicate that in the case of FP/BN nanohybrid, there is a large number of active sites responsible for the CO formation, while the number of active sites promoting the formation of CH species is less than that in the FO(P)/

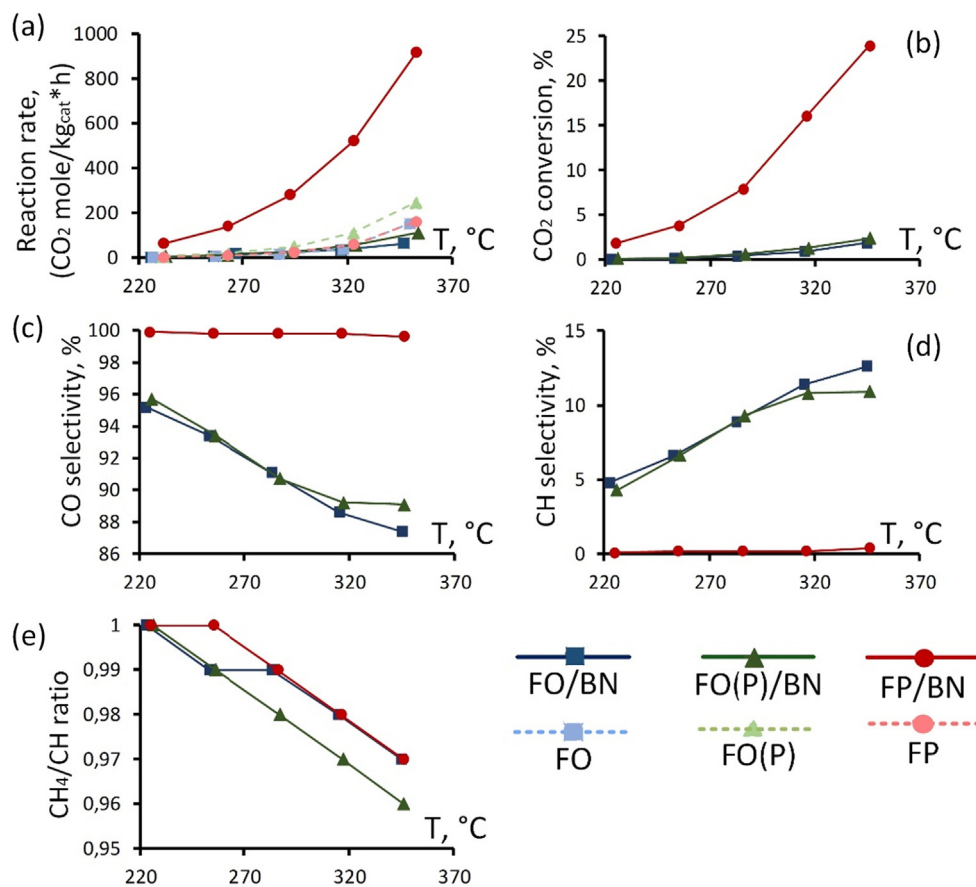


Fig. 5. Reaction rate (a) and CO conversion (b) related to: (c) CO selectivity, (d) hydrocarbons selectivity, and (e) methane ratio.

BN and FO/BN nanocomposites. This assumption can explain a decrease in the selectivity with respect to the CH species for the FP/BN sample. Since all materials demonstrate high selectivity toward CO, it is reasonable to assume that reverse water–gas shift (RWGS) reaction takes place during hydrogenation [71]. Carbon monoxide, as the first reaction product, can be further transformed into methanol and other hydrocarbons.

Table 3 compares the conversion, selectivity and productivity of various nanohybrids. Heterogeneous $\text{Fe}_3\text{O}_4/\text{h-BN}$ catalysts demonstrate the productivity similar to that of other heterogeneous materials based on iron and its compounds. Importantly, the FePt/BN nanohybrids exhibit improved catalytic performance even when compared to nanomaterials solely based on noble metals.

3.5. Nanoparticle stabilization mechanism

To study the role of *h*-BN support in the stabilization of catalytically active NPs the detailed TEM investigation was carried out. For that *in situ* annealing of the FP/BN sample in the TEM column was conducted. The obtained results are presented in Fig. 6.

As-synthesized FePt NPs have a narrow size distribution (1–2 nm size, Fig. 6a (inset)). After the *in situ* annealing the size distribution became wider (Fig. 6c (inset)), although most of the NPs

retained their small size (<10 nm). TEM analysis after *in situ* heating indicates that sintering of the FePt NPs starts approximately at 400 °C (Fig. 6b) and proceeds faster at higher temperatures (Fig. 6c). However, the TEM observation revealed that from a certain point the sintering process had almost stopped and the material microstructure remained relatively stable when heated at 900 °C for as long as 15 min (Fig. 6d). Even small FePt NPs located next to each other did not coagulate. Thorough TEM observation reveals that many FePt NPs are surrounded by a thin (2–4 atomic planes) layer of *h*-BN (Fig. 6e–g). This indicates the formation of core–shell *h*-BN@FePt NPs during heating that prevents FePt NPs from further sintering. The structure of FP/BN sample subjected to activation at 500 °C is shown in Fig. S4. A significant part of FePt NPs retained their size at less than 10 nm; however, individual larger NPs, up to 30 nm in size, are visible, which were formed as a result of sintering of smaller particles. It is also observed that a thin *h*-BN layer covers the surface of metallic NPs (Fig. S4b).

Sintering process is accompanied by NP migration over the BN surface. Thin *h*-BN nanosheets are curved and can be easily twisted around FePt NPs as they move along the surface (Fig. 7). In order to minimize the surface energy, final NP tends to maintain its spherical shape during sintering while becoming wrapped by a thin *h*-BN layer.

3.6. Molecular dynamic simulations

Interaction of Pt and Fe atoms was investigated for two different models using MD approach. In the first model, the ability of Pt NP to prevent Fe NP agglomerations was studied. For this, Fe NPs were placed on the surface of Pt NP (Fig. 8a). The system was subjected to heating from 300 K to 1300 K over 5 ns. The

Table 2
Specific surface area and TOF values.

Sample	BET Specific surface area, m ² /g	TOF at 350 °C, 10 ^{−2} s ^{−1}
FO/BN	273	0.64
FO(P)/BN	319	0.94
FP/BN	261	9.54

Table 3
Conversion, selectivity, and productivity of different catalysts

Source	Material	Preparation method	Activation	Exp. conditions	Conversion CO ₂ , %	Selectivity CO, %	Selectivity HC, %	Distribution of HC, C mol %			Productivity, mol CO ₂ *g _{cat} ⁻¹ *h ⁻¹
								C ₁	C ₂ - C ₄	C ₅	
This work	Fe ₃ O ₄ /BN	Polyol synthesis	H ₂ 500 °C 8 h	H ₂ :CO ₂ = 2:1; 40 L*gcat ⁻¹ ; 2 MPa; 350 °C	1.9	88.6	11.4	98.1	1.9	0.0	6.4 * 10 ⁻²
This work	Fe ₃ O ₄ (Pt)/BN	Polyol synthesis	H ₂ 500 °C 8 h	H ₂ :CO ₂ = 2:1; 40 L*gcat ⁻¹ ; 2 MPa; 350 °C	2.4	89.2	10.8	97.5	2.5	0.0	11.0 * 10 ⁻²
This work	FePt/BN	Polyol synthesis	H ₂ 500 °C 8 h	H ₂ :CO ₂ = 2:1; 40 L*gcat ⁻¹ ; 2 MPa; 350 °C	25	99.8	0.2	98.3	1.7	0.0	91.8 * 10 ⁻²
[72]	CuFeO ₂	Hydrothermal	H ₂ 400 °C 2 h	H ₂ :CO ₂ = 3:1; 1,8 L*gcat ⁻¹ ; 1 MPa; 300 °C	17.3	31.7	68.3	2.7	31.0	66.3	3.5 * 10 ⁻³
[73]	Fe–Zn–Zr@HZSM-5	Cladding	–	H ₂ :CO ₂ = 3:1; 3 L*gcat ⁻¹ ; 5 MPa; 340 °C	14.9	38.6	61.4	1.5	71.7	26.8	5.0 * 10 ⁻³
[74]	K-Fe/mZrO ₂	Solvothermal	H ₂ :N ₂ = 1:10 450 °C 4 h	H ₂ :CO ₂ = 4:1; 1.2 L*gcat ⁻¹ ; 2 MPa; 340 °C	23	12.0	88.0	75.0	25.0	–	2.5 * 10 ⁻³
[75]	CsFe/Al ₂ O ₃	Sequential wet impregnation	H ₂ :N ₂ = 1:9 800 °C 1 h	H ₂ :CO ₂ = 4:1; 12 L*gcat ⁻¹ ; 0.1 MPa; 400 °C	33.5	85.0	15.0	–	–	–	3.6 * 10 ⁻²
[76]	Fe–Cu/K/La/TiO ₂	Impregnation	H ₂ 400 °C 2 h	H ₂ :CO ₂ :Ar = 75:24:4; 3,6 L*gcat ⁻¹ ; 1.1 MPa; 300 °C	24.4	35.0	65.0	21.5	38.5	40.0	9.1 * 10 ⁻³
[77]	Fe–Cu–K/TiO ₂	Impregnation	H ₂ 400 °C 2 h	H ₂ :CO ₂ :Ar = 75:24:4; 3,6 L*gcat ⁻¹ ; 1.1 MPa; 300 °C	19.9	49.0	51.0	23.5	15.7	60.8	7.5 * 10 ⁻³
[78]	FeK/C	Triple incipient wetness impregnation	H ₂ 400 °C 4 h	H ₂ :CO ₂ = 2:1; 1.6 L*gcat ⁻¹ ; 2 MPa; 350 °C	24	40.0	60.0	25.0	41.7	33.3	5.7 * 10 ⁻³
[79]	Fe–K/La–Al ₂ O ₃	Impregnation	H ₂ 450 °C 24 h	H ₂ :CO ₂ :N ₂ = 73:24:3; 2 L*gcat ⁻¹ ; 1 MPa; 300 °C	24.5	37.5	62.5	11.8	30.3	57.9	5.3 * 10 ⁻³
[80]	Pt/CeO ₂	Impregnation	H ₂ :N ₂ = 65,8:34,2 300 °C 1 h	H ₂ :CO ₂ :N ₂ = 62,5:5:32,5; 48 L*gcat ⁻¹ ; 0.1 MPa; 250 °C	33	100.0	0.0	0.0	0.0	0.0	3.5 * 10 ⁻²
[81]	Pt/UiO-66	Solvothermal	–	H ₂ :CO ₂ = 5.2:1; 4.65 L*gcat ⁻¹ ; 0,1 MPa; 300 °C	32	77.0	23.0	23.0	0.0	0.0	1.1 * 10 ⁻²

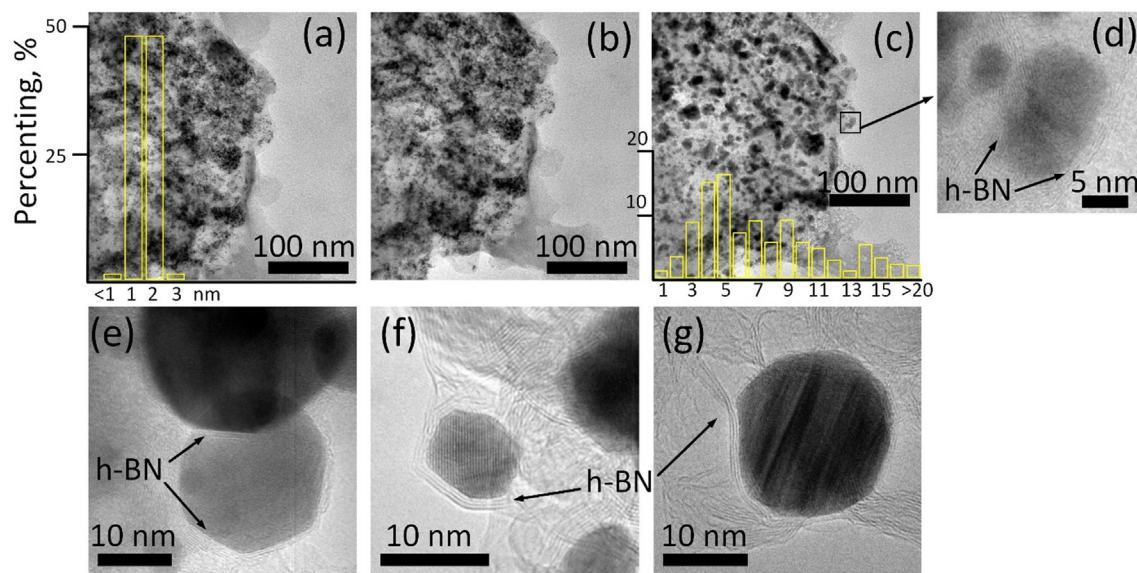


Fig. 6. TEM and HRTEM images of FP/BN materials (during *in situ* annealing): (a) TEM image at RT and FePt NP size distribution (inset); (b) TEM image at 400 °C; (c) TEM image at 700 °C and FePt NP size distribution (inset); (d) HRTEM image at 900 °C after exposure for 15 min; (e–g) HRTEM images of FePt NPs enveloped by *h*-BN nanosheets;

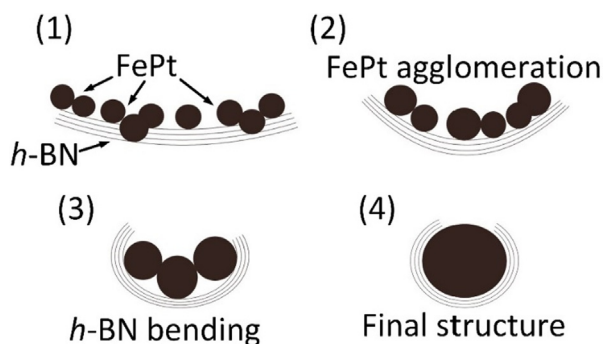


Fig. 7. Schematics of the FePt stabilization mechanism by *h*-BN layers.

obtained results indicate that during heating the Fe atoms do not form a shell around Pt NP and the diffusion of Fe atoms over the Pt surface is not significant. In contrast, Pt atoms can diffuse into the Fe NPs at high temperatures (Fig. 8b). Thus, the Pt NP can act as an anchor for the Fe NPs preventing their diffusion and agglomeration. Note that the Pt atom diffusion during heating is an important step toward bimetallic FePt NP formation.

Since the surface composition is a key factor influencing catalytic properties of the heterogeneous nanomaterials, the temperature-activated Pt atom diffusion to the surface of Fe NPs

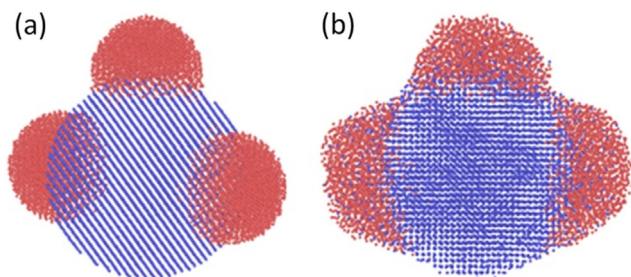


Fig. 8. Pt NP (blue colour) covered by Fe NPs (red colour): (a) before (300 K) and (b) after heating (1300 K). (For interpretation of the references to colour in this figure legend, the reader is referred to the web version of this article.)

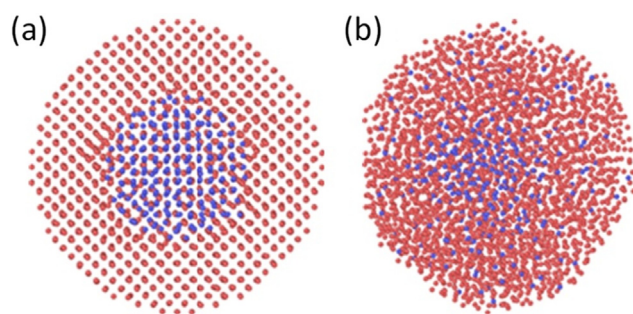


Fig. 9. Structure of 5 nm Fe@Pt NP with 10 at.% of Pt: (a) before ($T = 300$ K) and (b) after heating ($T = 1390$ K). Pt and Fe atoms marked by blue and red colours, respectively. (For interpretation of the references to colour in this figure legend, the reader is referred to the web version of this article.)

was further investigated in the frame of a core-shell Fe@Pt NP model (Fig. 9). The Fe@Pt NPs with a size of 5 and 10 nm were considered. The concentration of Pt in the core was 10 and 20 at.%. Fig. 9 depicts Fe@Pt NP with a diameter of 5 nm containing 10 at.% of Pt. The results indicate that Pt atoms tend to diffuse outwards through the Fe shell (Fig. 9b), this can lead to structural changes and phase transformations with the formation of FePt₃, FePt and Fe₃Pt phases.

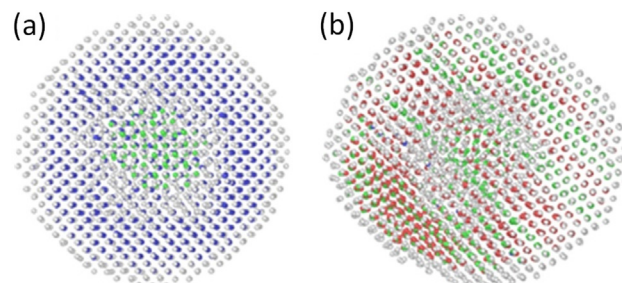


Fig. 10. The CNA of 5 nm Fe@Pt NP with 10 at.% of Pt: (a) before ($T = 300$ K) and (b) after heating ($T = 1390$ K). Bcc, fcc, hcp and amorphous phases are marked by blue, green, red, and white colours. (For interpretation of the references to colour in this figure legend, the reader is referred to the web version of this article.)

Table 4Temperature of $\text{Fe}_{\text{bcc}} \rightarrow \text{Fe}_{\text{fcc}}$ transition and melting temperatures of shell and core in the Fe@Pt NP vs NP size and Pt content in the core.

D, nm	Pt, %	T ($\text{Fe}_{\text{bcc}} \rightarrow \text{Fe}_{\text{fcc}}$), K	T _m (shell), K	T _m (core), K
5	10	670	1290	1390
5	20	575	1247	1392
10	10	815	1536	1583
10	20	690	1490	1650

The diffusion-induced structural transformation was further investigated using a Common Neighbor Analysis (CNA). For this, Fe@Pt NP with a diameter of 5 nm and containing 10% of Pt atoms was considered (Fig. 10). In the initial state, the Fe shell and Pt core had *bcc* and *fcc* structures, respectively. During heating at a temperature of 670 K, the $\text{Fe}_{\text{bcc}} \rightarrow \text{Fe}_{\text{fcc}}$ phase transformation occurs. Note, that the *fcc* Fe phase remains stable up to the melting point of $T_m = 1390$ K (Fig. 10b).

Table 4 summarizes the obtained results on the influence of NP size and Pt content in the core on the temperature of $\text{Fe}_{\text{bcc}} \rightarrow \text{Fe}_{\text{fcc}}$ transition and the melting temperature (T_m) of the core and the shell. With increasing Pt content to 20 %, the temperature of $\text{Fe}_{\text{bcc}} \rightarrow \text{Fe}_{\text{fcc}}$ transition decreases to 575 K (particle size 5 nm). A similar trend is observed for the 10 nm Fe@Pt NPs: the higher Pt content leads to the lower temperature of $\text{Fe}_{\text{bcc}} \rightarrow \text{Fe}_{\text{fcc}}$ transition. It should be noted that for larger NPs T_m of the core also rises with increasing Pt content (Table 4). In contrast, for smaller NPs (5 nm) T_m of the core is not affected by Pt content.

Based on MD simulations it can be concluded that the temperature of $\text{Fe}_{\text{bcc}} \rightarrow \text{Fe}_{\text{fcc}}$ phase transformation decreases with decreasing NP size and increasing Pt content while keeping the NP size constant. Further modeling of the chemical transformation was performed using DFT calculations.

3.7. Ab initio calculations

The calculation of sorption energy of the reactants, intermediate compounds, and reaction products was conducted by means of DFT. When modelling the FP nanoparticle, (111) Fe_3Pt surface as a slab with a size of $9.11 \times 5.26 \text{ \AA}$ consisting of 6 atomic layers was considered. Two bottom layers were frozen to simulate the bulk structure. The *k*-points mesh $6 \times 8 \times 1$ was used for optimization. To create an isolated surface, the vacuum space with a depth of 15 \AA was used. Based on the previous theoretical investigations of molecule sorption on a metal surface, the rPBE functional was selected [47]. The sorption energy E_{ads} was calculated as follows:

$$E_{\text{ads}} = E_{\text{mol_surf}} - E_{\text{mol}} - E_{\text{sub}}$$

where $E_{\text{mol_surf}}$ is the molecule energy adsorbed on the slab, E_{mol} is the energy of freestanding molecule, and E_{sub} is the energy of alloy

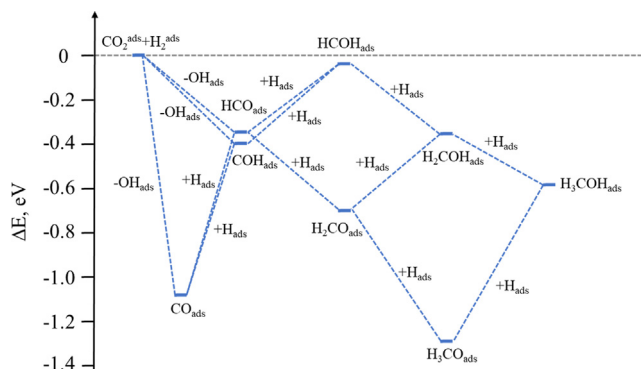
Table 5Sorption energy E_{ads} of the reactants, intermediate compounds and reaction products.

Compounds	E_{ads} , eV
CO_2	−0.08
2H	−0.90
H	−0.65
OH	−4.00
CO	−1.66
OCH	−2.33
COH	−4.21
CH_2O	−1.33
CHOH	−3.85
CH_2OH	−1.99
CH_3O	−3.24
CH_3OH	−0.54
H_2O	−0.61

slab. In order to confirm the correctness of the functional selection, the sorption energies of CO molecule to the Pt and Fe surfaces were calculated by using rPBE functional and applying Grimme corrections. The CO sorption energy on the Fe (111) surface was equal to -1.72 eV, which agrees well with the value of -1.75 eV reported elsewhere [82]. Good agreement between the calculated sorption values of CO on Pt(111) surface obtained in this work (-1.59 eV) and earlier reports ($E_{\text{ads}} = -1.59$ eV) [83] confirms the correctness of the selected functional.

The hydrogen dissociation barrier was calculated using the elastic band method [84–86]. The hydrogen molecule dissociation on the (111) Fe_3Pt surface occurs easily due to the low hydrogen dissociation barrier of 0.1 eV. This value is close to that calculated for Pt surface [87]. After the dissociation, two hydrogen atoms located in neighboring sorption centers have the energy of -0.45 eV/atom. This allows us to consider an individual hydrogen atom on the surface of Fe_3Pt as a reactant. The lowest sorption energy of a hydrogen atom is -0.65 eV/atom. In contrast, the calculated sorption energy of CO_2 molecule is -0.09 eV/mol, which is quite low and can only be attributed to the Van der Waals interactions. Therefore, at the initial stage, the CO_2 molecules will interact with atomic hydrogen and the reaction will follow the Eley-Rideal mechanism. Due to Sabatier principle, the reactant sorption energy and reaction-associated intermediate compounds affect catalytic processes. So, we also calculated the sorption energies of all possible transition structures and reaction products. The obtained results are collected in Table 5.

In order to estimate the possible reaction pathways, the calculated energy values are plotted relatively to adsorbed 2H and CO_2 on the (111) Fe_3Pt surface (Fig. 11). The interaction mechanism between CO_2 and hydrogen can be described as follows. Carbon monoxide is formed during the first reaction stage between carbon dioxide and hydrogen (Fig. 11). According to the experimental data, this is the main reaction product. Note that despite the relatively high sorption energy (-1.66 eV) of CO to Fe_3Pt surface, the formation of different hydrocarbons and alcohols is also possible. For example, formaldehyde is also seen among the reaction products (Fig. 11). Importantly, CH_2O amount should be rather low due to its relatively high sorption energy (-1.33 eV) preventing its output. As for other possible intermediate compounds, they

**Fig. 11.** Possible reaction pathways.

all have low sorption energies (Table 5), which may be due to the presence of dangling bonds that are saturated during their interaction with the Fe₃Pt surface. The H₂O and methanol molecules can be formed during the reaction since they both have low sorption energies (−0.61 and −0.54 eV, respectively). As a result, they can easily detach from the catalyst surface. Since the sorption energy of carbon monoxide is relatively high, it can be converted to hydrocarbons on the catalyst surface *via* reaction with atomic hydrogen. With a hydrogen atom added, the resulting HCO and COH products have a low sorption energy and can decompose into CO and hydrogen. This may explain the high yield of CO.

4. Conclusions

Novel Fe₃O₄/BN, Fe₃O₄(Pt)/BN, and FePt/BN heterogeneous nanomaterials have been fabricated *via* polyol synthesis and characterized with respect to their catalytic performance in CO₂ hydrogenation reaction. Their catalytic behaviour has been compared with unsupported Fe₃O₄, Fe₃O₄(Pt), and FePt NPs. The important findings are:

- 1) In Pt-free media, Fe₃O₄ NPs with a wide size distribution are formed on the *h*-BN surface. With increasing Pt content, the NP size first decreases, particle distribution becomes narrower, and then bimetallic FePt NPs are formed.
- 2) *In situ* TEM analysis shows the formation of core-shell *h*-BN@FePt NPs during heating that prevents FePt NPs from further sintering during the catalytic process.
- 3) The FePt/BN nanomaterial with bimetallic FePt NPs shows a significantly higher CO₂ conversion rate as compared to the Fe₃O₄/BN and Fe₃O₄(Pt)/BN heterogeneous nanomaterials and BN-free NPs. In addition, the FePt/BN catalysts exhibit almost 100% selectivity to carbon monoxide. In contrast, the Fe₃O₄/BN and Fe₃O₄(Pt)/BN nanomaterials appear to be more promising catalysts for hydrocarbon production despite lower conversion and reaction rate.
- 4) Molecular dynamic simulations indicate that (i) Pt NP can act as an anchor for Fe NPs preventing their diffusion and agglomeration, (ii) Pt atoms tend to diffuse outwards through the Fe shell, and (iii) Pt encourages the temperature-activated Fe_{bcc} → Fe_{fcc} phase transformation.
- 5) The possible reaction pathways including carbon monoxide formation during carbon dioxide and hydrogen interaction are elucidated based on the calculated sorption energies of all reactants, intermediate compounds and reaction products.

Our findings can provide a basis for the development of novel efficient catalysts through exploiting the reported unique interactions between the components.

Declaration of Competing Interest

The authors declare that they have no known competing financial interests or personal relationships that could have appeared to influence the work reported in this paper.

Acknowledgements

The authors gratefully acknowledge the financial support from the Russian Science Foundation (Agreement No. 20-79-10286) in the part of catalyst fabrication, characterization, and testing in CO₂ hydrogenation reaction and the Ministry of Education and Science of the Russian Federation (Increase Competitiveness Program of NUST «MISI» No. K2-2020-009) in the part of theoretical

calculations. D.G. is grateful to the Australian Research Council (ARC) for granting a Laureate Fellowship FL160100089.

Appendix A. Supplementary material

Supplementary data to this article can be found online at <https://doi.org/10.1016/j.jcat.2021.08.026>.

References

- [1] C.D. Thomas, A. Cameron, R.E. Green, M. Bakkenes, L.J. Beaumont, Y.C. Collingham, B.F.N. Erasmus, M.F. de Siqueira, A. Grainger, L. Hannah, L. Hughes, B. Huntley, A.S. van Jaarsveld, G.F. Midgley, L. Miles, M.A. Ortega-Huerta, A. Townsend Peterson, O.L. Phillips, S.E. Williams, Extinction risk from climate change, *Nature* 427 (6970) (2004) 145–148, <https://doi.org/10.1038/nature02121>.
- [2] C. Le Quéré, R.M. Andrew, P. Friedlingstein, S. Sitch, J. Pongratz, A.C. Manning, J. Ivar Korsbakken, G.P. Peters, J.G. Canadell, R.B. Jackson, T.A. Boden, P.P. Tans, O. D. Andrews, V.K. Arora, D.C.E. Bakker, L. Barbero, M. Becker, R.A. Betts, L. Bopp, F. Chevallier, L.P. Chini, P. Ciais, C.E. Cosca, J. Cross, K. Currie, T. Gasser, I. Harris, J. Hauck, V. Haverd, R.A. Houghton, C.W. Hunt, G. Hurtt, T. Ilyina, A.K. Jain, E. Kato, M. Kautz, R.F. Keeling, K. Klein Goldewijk, A. Körtzinger, P. Landschützer, N. Lefèvre, A. Lenton, S. Lienert, I. Lima, D. Lombardozzi, N. Metz, F. Millero, P. M.S. Monteiro, D.R. Munro, J.E.M.S. Nabel, S.I. Nakaoka, Y. Nojiri, X. Antonio Padin, A. Peregon, B. Pfeil, D. Pierrot, B. Poulter, G. Rehder, J. Reimer, C. Rödenbeck, J. Schwinger, R. Séférian, I. Skjelvan, B.D. Stocker, H. Tian, B. Tilbrook, F.N. Tubiello, I.T.V. Laan-Luijckx, G.R.V. Werf, S. Van Heuven, N. Viovy, N. Vuichard, A.P. Walker, A.J. Watson, A.J. Wiltshire, S. Zaehle, D. Zhu, Global Carbon Budget 2017, *Earth Syst. Sci. Data* 10 (2018) 405–448, doi:10.5194/essd-10-405-2018.
- [3] A.E. Raftery, A. Zimmer, D.M.W. Frierson, R. Startz, P. Liu, Less than 2°C warming by 2100 unlikely, *Nat. Clim. Chang.* 7 (2017) 637–641, <https://doi.org/10.1038/nclimate3352>.
- [4] F.V. Bekun, A.A. Alola, S.A. Sarkodie, Toward a sustainable environment: Nexus between CO₂ emissions, resource rent, renewable and nonrenewable energy in 16-EU countries, *Sci. Total Environ.* 657 (2019) 1023–1029, <https://doi.org/10.1016/j.scitotenv.2018.12.104>.
- [5] W. Li, H. Wang, X. Jiang, J. Zhu, Z. Liu, X. Guo, C. Song, A short review of recent advances in CO₂ hydrogenation to hydrocarbons over heterogeneous catalysts, *RSC Adv.* 8 (14) (2018) 7651–7669, <https://doi.org/10.1039/C7RA13546G>.
- [6] J. Artz, T.E. Müller, K. Thenert, J. Kleinekorte, R. Meys, A. Sternberg, A. Bardow, W. Leitner, Sustainable conversion of carbon dioxide: an integrated review of catalysis and life cycle assessment, *Chem. Rev.* 118 (2) (2018) 434–504, <https://doi.org/10.1021/acs.chemrev.7b00435>.
- [7] M. Bui, C.S. Adjiman, A. Bardow, E.J. Anthony, A. Boston, S. Brown, P.S. Fennell, S. Fuss, A. Galindo, L.A. Hackett, J.P. Hallett, H.J. Herzog, G. Jackson, J. Kemper, S. Krevor, G.C. Maitland, M. Matuszewski, I.S. Metcalfe, C. Petit, G. Puxty, J. Reimer, D.M. Reiner, E.S. Rubin, S.A. Scott, N. Shah, B. Smit, J.P.M. Trusler, P. Webley, J. Wilcox, N. Mac Dowell, Carbon capture and storage (CCS): The way forward, *Energy Environ. Sci.* 11 (5) (2018) 1062–1176, <https://doi.org/10.1039/C7EE02342A>.
- [8] C. Liang, L. Pan, S. Liang, Y. Xia, Z. Liang, Y. Gan, H. Huang, J. Zhang, W. Zhang, Ultraefficient conversion of CO₂ into morphology-controlled nanocarbons: a sustainable strategy toward greenhouse gas utilization, *Small* 15 (33) (2019) 1902249, <https://doi.org/10.1002/smll.v15.3310.1002/smll.201902249>.
- [9] A.H. Assen, Y. Belmabkhout, K. Adil, A. Lachehab, H. Hassoune, H. Aggarwal, Advances on CO₂ storage. Synthetic porous solids, mineralization and alternative solutions, *Chem. Eng. J.* 419 (2021) 129569, <https://doi.org/10.1016/j.cej.2021.129569>.
- [10] T. Billo, F.-Y. Fu, P. Raghunath, I. Shown, W.-F. Chen, H.-T. Lien, T.-H. Shen, J.-F. Lee, T.-S. Chan, K.-Y. Huang, C.-I. Wu, M.C. Lin, J.-S. Hwang, C.-H. Lee, L.-C. Chen, K.-H. Chen, Ni-nanocluster modified black TiO₂ with dual active sites for selective photocatalytic CO₂ reduction, *Small* 14 (2) (2018) 1702928, <https://doi.org/10.1002/smll.v14.210.1002/smll.201702928>.
- [11] N. Meiri, R. Radus, M. Herskowitz, Simulation of novel process of CO₂ conversion to liquid fuels, *J. CO₂ Util.* 17 (2017) 284–289, <https://doi.org/10.1016/j.jcou.2016.12.008>.
- [12] J. Jin, J. Yu, D. Guo, C. Cui, W. Ho, A Hierarchical Z-scheme CdS-WO₃ photocatalyst with enhanced CO₂ reduction activity, *Small* 11 (39) (2015) 5262–5271, <https://doi.org/10.1002/smll.201500926>.
- [13] J. Fu, B. Zhu, C. Jiang, B. Cheng, W. You, J. Yu, Hierarchical porous O-doped g-C₃N₄ with enhanced photocatalytic CO₂ reduction activity, *Small* 13 (15) (2017) 1603938, <https://doi.org/10.1002/smll.v13.1510.1002/smll.201603938>.
- [14] A.D.N. Kamkeng, M. Wang, J. Hu, W. Du, F. Qian, Transformation technologies for CO₂ utilisation: Current status, challenges and future prospects, *Chem. Eng. J.* 409 (2021) 128138, <https://doi.org/10.1016/j.cej.2020.128138>.
- [15] H. Yang, C. Zhang, P. Gao, H. Wang, X. Li, L. Zhong, W. Wei, Y. Sun, A review of the catalytic hydrogenation of carbon dioxide into value-added hydrocarbons, *Catal. Sci. Technol.* 7 (20) (2017) 4580–4598, <https://doi.org/10.1039/C7CY01403A>.
- [16] R. Arenal, M.S. Wang, Z. Xu, A. Loiseau, D. Golberg, Young's modulus, mechanical and electrical properties of isolated individual and bundled

- single-walled boron nitride nanotubes, *Nanotechnology* 22 (2011), <https://doi.org/10.1088/0957-4484/22/26/265704>.
- [17] D. Golberg, Y. Bando, K. Kurashima, T. Sato, Synthesis and characterization of ropes made of BN multiwalled nanotubes, *Scr. Mater.* 44 (8–9) (2001) 1561–1565, [https://doi.org/10.1016/S1359-6462\(01\)00724-2](https://doi.org/10.1016/S1359-6462(01)00724-2).
 - [18] D.V. Shtansky, K.L. Firestein, D.V. Golberg, Fabrication and application of BN nanoparticles, nanosheets and their nanohybrids, *Nanoscale* 10 (37) (2018) 17477–17493, <https://doi.org/10.1039/C8NR05027A>.
 - [19] A.T. Matveev, K.L. Firestein, A.E. Steinman, A.M. Kovalskii, I.V. Sukhorukova, O. I. Lebedev, D.V. Shtansky, D. Golberg, Synthesis of boron nitride nanostructures from borates of alkali and alkaline earth metals, *J. Mater. Chem. A* 3 (41) (2015) 20749–20757, <https://doi.org/10.1039/C5TA05831G>.
 - [20] F. Ersan, G. Gökoglu, E. Aktürk, Bimetallic two-dimensional PtAg coverage on h-BN substrate: First-principles calculations, *Appl. Surf. Sci.* 303 (2014) 306–311, <https://doi.org/10.1016/j.apsusc.2014.02.171>.
 - [21] Z. Lu, P. Lv, Z. Yang, S. Li, D. Ma, R. Wu, A promising single atom catalyst for CO oxidation: Ag on boron vacancies of h-BN sheets, *Phys. Chem. Chem. Phys.* 19 (25) (2017) 16795–16805, <https://doi.org/10.1039/C7CP02430D>.
 - [22] X. Wang, Z. Yan, H. Zhou, X. Zhang, J. Jia, H. Wu, O₂ activation and CO oxidation on n-p codoped h-BN single-atom catalysts, *Comput. Theor. Chem.* 1127 (2018) 31–36, <https://doi.org/10.1016/j.comptc.2018.01.020>.
 - [23] A.S. Konopatsky, D.V. Leybo, K.L. Firestein, Z.I. Popov, A.V. Bondarev, A.M. Manakhov, E.S. Permyakova, D.V. Shtansky, D.V. Golberg, Synthetic routes, structure and catalytic activity of Ag/BN nanoparticle hybrids toward CO oxidation reaction, *J. Catal.* 368 (2018) 217–227, <https://doi.org/10.1016/j.jcat.2018.10.016>.
 - [24] K.L. Firestein, D.V. Leybo, A.E. Steinman, A.M. Kovalskii, A.T. Matveev, A.M. Manakhov, I.V. Sukhorukova, P.V. Slukin, N.K. Fursova, S.G. Ignatov, D.V. Golberg, D.V. Shtansky, BN/Ag hybrid nanomaterials with petal-like surfaces as catalysts and antibacterial agents, *Beilstein J. Nanotechnol.* 9 (2018) 250–261, <https://doi.org/10.3762/bjnano.9.27>.
 - [25] K. Vikanova, E. Redina, G. Kapustin, V. Nissenbaum, I. Mishin, E. Kostyukhin, L. Kustov, Template-free one-step synthesis of micro-mesoporous CeO₂–ZrO₂ mixed oxides with a high surface area for selective hydrogenation, *Ceram. Int.* 46 (9) (2020) 13980–13988, <https://doi.org/10.1016/j.ceramint.2020.02.197>.
 - [26] Y. Du, C. Qin, Y. Xu, D. Xu, J. Bai, G. Ma, M. Ding, Ni nanoparticles dispersed on oxygen vacancies-rich CeO₂ nanoparticles for enhanced low-temperature CO₂ methanation performance, *Chem. Eng. J.* 418 (2021) 129402, <https://doi.org/10.1016/j.cej.2021.129402>.
 - [27] K. Samson, M. Šliwa, R.P. Socha, K. Góra-Marek, D. Mucha, D. Rutkowska-Zbik, J.-F. Paul, M. Ruggiero-Mikołajczyk, R. Grabowski, J. Słoczyński, Influence of ZrO₂ structure and copper electronic state on activity of Cu/ZrO₂ catalysts in methanol synthesis from CO₂, *ACS Catal.* 4 (10) (2014) 3730–3741, <https://doi.org/10.1021/cs500979c>.
 - [28] A.S. Konopatsky, K.L. Firestein, D.V. Leybo, Z.I. Popov, K.V. Larionov, A.E. Steinman, A.M. Kovalskii, A.T. Matveev, A.M. Manakhov, P.B. Sorokin, D. Golberg, D.V. Shtansky, BN Nanoparticle/Ag hybrids with enhanced catalytic activity: theory and experiments, *Catal. Sci. Technol.* 8 (6) (2018) 1652–1662, <https://doi.org/10.1039/C7CY02207G>.
 - [29] S.O. Moussa, L.S. Panchakarla, M.Q. Ho, M.S. El-Shall, Graphene-supported, iron-based nanoparticles for catalytic production of liquid hydrocarbons from synthesis gas: the role of the graphene support in comparison with carbon nanotubes, *ACS Catal.* 4 (2) (2014) 535–545, <https://doi.org/10.1021/cs4010198>.
 - [30] D. Huber, Synthesis, properties, and applications of iron nanoparticles, *Small* 1 (5) (2005) 482–501, [https://doi.org/10.1002/\(ISSN\)1613-682910.1002/sml.v1:510.1002/sml.200500006](https://doi.org/10.1002/(ISSN)1613-682910.1002/sml.v1:510.1002/sml.200500006).
 - [31] F. Jiang, B. Liu, S. Geng, Y. Xu, X. Liu, Hydrogenation of CO₂ into hydrocarbons: enhanced catalytic activity over Fe-based Fischer-Tropsch catalysts, *Catal. Sci. Technol.* 8 (16) (2018) 4097–4107, <https://doi.org/10.1039/C8CY00850G>.
 - [32] C. Yang, S. Li, Z. Zhang, H. Wang, H. Liu, F. Jiao, Z. Guo, X. Zhang, W. Hu, Organic-inorganic hybrid nanomaterials for electrocatalytic CO₂ reduction, *Small* 16 (29) (2020) 2001847, <https://doi.org/10.1002/sml.v16.2910.1002/sml.202001847>.
 - [33] B. Liang, H. Duan, T. Sun, J. Ma, X. Liu, J. Xu, X. Su, Y. Huang, T. Zhang, Effect of Na promoter on Fe-based catalyst for CO₂ hydrogenation to alkenes, *ACS Sustain. Chem. Eng.* 7 (1) (2019) 925–932, <https://doi.org/10.1021/acssuschemeng.8b0453810.1021/acssuschemeng.8b0453810.1021/acssuschemeng.8b0453810>.
 - [34] M. Dad, H.O.A. Fredriksson, J. Van de Loosdrecht, P.C. Thüne, J.W. Niemantsverdriet, Stabilization of iron by manganese promoters in uniform bimetallic FeMn Fischer-Tropsch model catalysts prepared from colloidal nanoparticles, *Catal. Struct. React.* 1 (2) (2015) 101–109, <https://doi.org/10.1179/2055075815Y.0000000003>.
 - [35] T. Dong, H. Luo, Y. Wang, B. Hu, H. Chen, Stabilization of Fe-Pd bimetallic nanoparticles with sodium carboxymethyl cellulose for catalytic reduction of para-nitrochlorobenzene in water, *Desalination* 271 (1–3) (2011) 11–19, <https://doi.org/10.1016/j.desal.2010.12.003>.
 - [36] S. Valange, R. Palacio, A. Charnot, J. Barrault, A. Louati, Z. Gabelica, Nanoparticles of Fe₂O₃ inserted in SBA-15 silica at micropore mouth level: an experimental evidence of the confinement effect, *J. Mol. Catal. A Chem.* 305 (1–2) (2009) 24–33, <https://doi.org/10.1016/j.molcata.2009.03.001>.
 - [37] X. Xu, Z. Xu, B. Gao, L. Zhao, Y. Zheng, J. Huang, D.C.W. Tsang, Y.S. Ok, X. Cao, New insights into CO₂ sorption on biochar/Fe oxyhydroxide composites: kinetics, mechanisms, and *in situ* characterization, *Chem. Eng. J.* 384 (2020) 123289, <https://doi.org/10.1016/j.cej.2019.123289>.
 - [38] R.J. Joseyphus, K. Shinoda, D. Kodama, B. Jeyadevan, Size controlled Fe nanoparticles through polyol process and their magnetic properties, *Mater. Chem. Phys.* 123 (2–3) (2010) 487–493, <https://doi.org/10.1016/j.matchemphys.2010.05.001>.
 - [39] S. Plimpton, Fast parallel algorithms for short-range molecular dynamics, *J. Comput. Phys.* 117 (1) (1995) 1–19, <https://doi.org/10.1006/jcph.1995.1039>.
 - [40] M. Müller, P. Erhart, K. Albe, Analytic bond-order potential for bcc and fcc iron – comparison with established embedded-atom method potentials, *J. Phys. Condens. Matter.* 19 (32) (2007) 326220, <https://doi.org/10.1088/0953-8984/19/32/326220>.
 - [41] M. Müller, K. Albe, Structural stability of multiply twinned FePt nanoparticles, *Acta Mater.* 55 (19) (2007) 6617–6626, <https://doi.org/10.1016/j.actamat.2007.08.030>.
 - [42] A.K. Rajagopal, J. Callaway, Inhomogeneous electron gas, *Phys. Rev. B* 7 (5) (1973) 1912–1919, <https://doi.org/10.1103/PhysRevB.7.1912>.
 - [43] W. Kohn, L.J. Sham, Self-consistent equations including exchange and correlation effects, *Phys. Rev.* 140 (4A) (1965) A1133–A1138, <https://doi.org/10.1103/PhysRev.140.A1133>.
 - [44] G. Kresse, J. Furthmüller, Efficient iterative schemes for *ab initio* total-energy calculations using a plane-wave basis set, *Phys. Rev. B - Condens. Matter Mater. Phys.* 54 (16) (1996) 11169–11186, <https://doi.org/10.1103/PhysRevB.54.11169>.
 - [45] G. Kresse, J. Furthmüller, Efficiency of *ab-initio* total energy calculations for metals and semiconductors using a plane-wave basis set, *Comput. Mater. Sci.* 6 (1) (1996) 15–50, [https://doi.org/10.1016/0927-0256\(96\)00008-0](https://doi.org/10.1016/0927-0256(96)00008-0).
 - [46] G. Kresse, J. Hafner, *Ab initio* molecular dynamics for liquid metals, *Phys. Rev. B* 47 (1) (1993) 558–561, <https://doi.org/10.1103/PhysRevB.47.558>.
 - [47] B. Hammer, L.B. Hansen, J.K. Nørskov, Improved adsorption energetics within density-functional theory using revised Perdew-Burke-Ernzerhof functionals, *Phys. Rev. B - Condens. Matter Mater. Phys.* 59 (11) (1999) 7413–7421, <https://doi.org/10.1103/PhysRevB.59.7413>.
 - [48] Z. Liu, C. Wu, L. Niu, G. Yang, K. Wang, W. Pei, Q. Wang, Post-treatment method for the synthesis of monodisperse binary FePt-Fe₃O₄ nanoparticles, *Nanoscale Res. Lett.* 12 (2017) 2–7, <https://doi.org/10.1186/s11671-017-2312-5>.
 - [49] H.L. Nguyen, L.E.M. Howard, G.W. Stinton, S.R. Giblin, B.K. Tanner, I. Terry, A.K. Hughes, I.M. Ross, A. Serres, J.S.O. Evans, Synthesis of size-controlled fcc and fct FePt nanoparticles, *Chem. Mater.* 18 (26) (2006) 6414–6424, <https://doi.org/10.1021/cm062127e10.1021/cm062127e.s001>.
 - [50] E. Da Silva Nunes, W.R. Viali, S.W. Da Silva, J.A.H. Coaquira, V.K. Garg, A.C. De Oliveira, P.C. Moraes, M. Jafelici, Characterization of tetraethylene glycol passivated iron nanoparticles, *Appl. Surf. Sci.* 315 (2014) 337–345, <https://doi.org/10.1016/j.apsusc.2014.07.154>.
 - [51] X. Li, L. An, X. Wang, F. Li, R. Zou, D. Xia, Supported sub-5 nm Pt-Fe intermetallic compounds for electrocatalytic application, *J. Mater. Chem.* 22 (2012) 6047–6052, <https://doi.org/10.1039/c2jm16504j>.
 - [52] M.F. Wenjuan Lei, Y.u. Yongsheng, W. Yang, H. Li, A general strategy for synthesizing high-coercivity L10-FePt, *Nanoscale* (2017) 12855–12861, <https://doi.org/10.1039/C7NR04849A>.
 - [53] N.K. Sahu, J. Gupta, D. Bahadur, PEGylated FePt-Fe₃O₄ composite nanoassemblies (CNAs): *In vitro* hyperthermia, drug delivery and generation of reactive oxygen species (ROS), *Dalt. Trans.* 44 (19) (2015) 9103–9113, <https://doi.org/10.1039/C4DT03470H>.
 - [54] A.S. Konopatsky, K.L. Firestein, D.V. Leybo, E.V. Sukhanova, Z.I. Popov, X. Fang, A.M. Manakhov, A.M. Kovalskii, A.T. Matveev, D.V. Shtansky, D.V. Golberg, Structural evolution of Ag/BN hybrids via a polyol-assisted fabrication process and their catalytic activity in CO oxidation, *Catal. Sci. Technol.* 9 (22) (2019) 6460–6470, <https://doi.org/10.1039/C9CY01464K>.
 - [55] N. Kumar Sahu, D. Bahadur, Influence of excess Fe accumulation over the surface of FePt nanoparticles: structural and magnetic properties, *J. Appl. Phys.* 113 (13) (2013) 134303, <https://doi.org/10.1063/1.4796091>.
 - [56] P. de la Presa, T. Rueda, A. Hernandez, J.M. Ramallo-López, L.J. Giovanetti, F.G. Requejo, Spontaneous oxidation of disordered fcc FePt nanoparticles, *J. Appl. Phys.* 103 (10) (2008) 103909, <https://doi.org/10.1063/1.2931947>.
 - [57] F. Han, L. Ma, Q. Sun, C. Lei, A. Lu, Rationally designed carbon-coated Fe₃O₄ coaxial nanotubes with hierarchical porosity as high-rate anodes for lithium ion batteries, *Nano Res.* 7 (11) (2014) 1706–1717, <https://doi.org/10.1007/s12274-014-0531-y>.
 - [58] M. Murugesan, J.C. Bea, C.-K. Yin, H. Nohira, E. Ikenaga, T. Hattori, M. Nishijima, T. Fukushima, T. Tanaka, M. Miyao, M. Koyanagi, Investigation of the effect of *in situ* annealing of FePt nanodots under high vacuum on the chemical states of Fe and Pt by X-ray photoelectron spectroscopy, *J. Appl. Phys.* 104 (7) (2008) 074316, <https://doi.org/10.1063/1.2973665>.
 - [59] J. Lee, J.M. Yoo, Y. Ye, Y. Mun, S. Lee, O.-H. Kim, H.-W. Rhee, H.I. Lee, Y.-E. Sung, J. Lee, Development of highly stable and mass transfer-enhanced cathode catalysts: support-free electrospun intermetallic FePt nanotubes for polymer electrolyte membrane fuel cells, *Adv. Energy Mater.* 5 (11) (2015) 1402093, <https://doi.org/10.1002/aenm.v5.1110.1002/aenm.201402093>.
 - [60] S. Alayoglu, S.K. Beaumont, F. Zheng, V.V. Pushkarev, H. Zheng, V. Iablokov, Z. Liu, J. Guo, N. Kruse, G.A. Somorjai, CO₂ hydrogenation studies on Co and CoPt bimetallic nanoparticles under reaction conditions using TEM, XPS and NEXAFS, *Top. Catal.* 54 (13–15) (2011) 778–785, <https://doi.org/10.1007/s11244-011-9695-9>.
 - [61] W.K. Jozwiak, E. Kaczmarek, T.P. Maniecki, W. Ignaczak, W. Maniukiewicz, Reduction behavior of iron oxides in hydrogen and carbon monoxide atmospheres, *Appl. Catal. A Gen.* 326 (1) (2007) 17–27, <https://doi.org/10.1016/j.apcata.2007.03.021>.

- [62] O.A. Teylov, Kinetics of the low-temperature hydrogen reduction of magnetite concentrates, *Russ. Metall.* 2012 (1) (2012) 8–21, <https://doi.org/10.1134/S0036029512010132>.
- [63] D. Spreitzer, J. Schenk, Reduction of iron oxides with hydrogen—a review, *Steel Res. Int.* 90 (10) (2019) 1900108, <https://doi.org/10.1002/srin.v90.1010.1002/srin.201900108>.
- [64] A. Pineau, N. Kanari, I. Gaballah, Kinetics of reduction of iron oxides by H₂. Part II. Low temperature reduction of magnetite, *Thermochim. Acta* 456 (2) (2007) 75–88, <https://doi.org/10.1016/j.tca.2007.01.014>.
- [65] B. Hou, H. Zhang, H. Li, Q. Zhu, Study on kinetics of iron oxide reduction by hydrogen, *Chinese J. Chem. Eng.* 20 (1) (2012) 10–17, [https://doi.org/10.1016/S1004-9541\(12\)60357-7](https://doi.org/10.1016/S1004-9541(12)60357-7).
- [66] Z. Chen, J. Dang, X. Hu, H. Yan, Reduction kinetics of hematite powder in hydrogen atmosphere at moderate temperatures, *Metals* 8 (10) (2018) 751, <https://doi.org/10.3390/met8100751>.
- [67] T. Riedel, H. Schulz, G. Schaub, K.-W. Jun, J.-S. Hwang, K.-W. Lee, Fischer-Tropsch on iron with H₂/CO and H₂/CO₂ as synthesis gases: the episodes of formation of the Fischer-Tropsch regime and construction of the catalyst, *Top. Catal.* 26 (1–4) (2003) 41–54, <https://doi.org/10.1023/B:TOCA.0000012986.46680.28>.
- [68] J.-F. Lee, W.-S. Chern, M.-D. Lee, T.-Y. Dong, Hydrogenation of carbon dioxide on iron catalysts doubly promoted with manganese and potassium, *Can. J. Chem. Eng.* 70 (1992) 511–515, <https://doi.org/10.1002/cjce.5450700314>.
- [69] W. Wang, S. Wang, X. Ma, J. Gong, Recent advances in catalytic hydrogenation of carbon dioxide, *Chem. Soc. Rev.* 40 (2011) 3703–3727, <https://doi.org/10.1039/c1cs15008a>.
- [70] M.D. Porosoff, J.G. Chen, Trends in the catalytic reduction of CO₂ by hydrogen over supported monometallic and bimetallic catalysts, *J. Catal.* 301 (2013) 30–37, <https://doi.org/10.1016/j.jcat.2013.01.022>.
- [71] L. Pastor-Pérez, F. Baibars, E. Le Sache, H. Arellano-García, S. Gu, T.R. Reina, CO₂ valorisation via reverse water-gas shift reaction using advanced Cs doped Fe-Cu/Al₂O₃ catalysts, *J. CO₂ Util.* 21 (2017) 423–428, <https://doi.org/10.1016/j.jcou.2017.08.009>.
- [72] Y.H. Choi, Y.J. Jang, H. Park, W.Y. Kim, Y.H. Lee, S.H. Choi, J.S. Lee, Carbon dioxide Fischer-Tropsch synthesis: a new path to carbon-neutral fuels, *Appl. Catal. B Environ.* 202 (2017) 605–610, <https://doi.org/10.1016/j.apcatb.2016.09.072>.
- [73] Xiaoxing Wang, Guohui Yang, Junfeng Zhang, Shuyao Chen, Yingquan Wu, Qingde Zhang, Junwei Wang, Yizhuo Han, Yisheng Tan, Synthesis of isoalkanes over a core (Fe-Zn-Zr)-shell (zeolite) catalyst by CO₂ hydrogenation, *Chem. Commun.* 52 (46) (2016) 7352–7355, <https://doi.org/10.1039/C6CC01965J>.
- [74] Hao Gu, Jie Ding, Qin Zhong, Yiqing Zeng, Fujiao Song, Promotion of surface oxygen vacancies on the light olefins synthesis from catalytic CO₂ hydrogenation over FeK/ZrO₂ catalysts, *Int. J. Hydrogen Energy* 44 (23) (2019) 11808–11816, <https://doi.org/10.1016/j.ijhydene.2019.03.046>.
- [75] Laura Pastor-Pérez, Mihir Shah, Estelle le Saché, Tomas Ramirez Reina, Improving Fe/Al₂O₃ catalysts for the reverse water-gas shift reaction: on the effect of Cs as activity/selectivity promoter, *Catalysts* 8 (12) (2018) 608, <https://doi.org/10.3390/catal8120608>.
- [76] Nuttakorn Boreriboon, Xiao Jiang, Chunshan Song, Pattarapan Prasassarakich, Higher hydrocarbons synthesis from CO₂ hydrogenation over K- and La-promoted Fe-Cu/TiO₂ catalysts, *Top. Catal.* 61 (15–17) (2018) 1551–1562, <https://doi.org/10.1007/s11244-018-1023-1>.
- [77] N. Boreriboon, X. Jiang, C. Song, P. Prasassarakich, Fe-based bimetallic catalysts supported on TiO₂ for selective CO₂ hydrogenation to hydrocarbons, *J. CO₂ Util.* 25 (2018) 330–337, <https://doi.org/10.1016/j.jcou.2018.02.014>.
- [78] Ya.A. Pokusaeva, A.E. Koklin, O.L. Eliseev, R.V. Kazantsev, V.I. Bogdan, Hydrogenation of carbon oxides over the Fe-based catalysts on the carbon support, *Russ. Chem. Bull.* 69 (2) (2020) 237–240, <https://doi.org/10.1007/s11172-020-2751-5>.
- [79] L. Zhang, H. Wang, C. Yang, X. Li, J. Sun, H. Wang, P. Gao, Y. Sun, The rare earth elements modified FeK/Al₂O₃ catalysts for direct CO₂ hydrogenation to liquid hydrocarbons, *Catal. Today* 356 (2020) 613–621, <https://doi.org/10.1016/j.cattod.2019.11.006>.
- [80] Yuan Wang, Hamidreza Arandiyani, Jason Scott, Kondo-Francois Aguey-Zinsou, Rose Amal, Single atom and nanoclustered Pt catalysts for selective CO₂ reduction, *ACS Appl. Energy Mater.* 1 (12) (2018) 6781–6789, <https://doi.org/10.1021/acsaeam.8b0081710.1021/acsaeam.8b00817.s001>.
- [81] Maria Mihet, Gabriela Blanita, Monica Dan, Lucian Barbu-Tudoran, Mihaela D Lazar, Pt/UiO-66 nanocomposites as catalysts for CO₂ methanation process, *J. Nanosci. Nanotechnol.* 19 (6) (2019) 3187–3196, <https://doi.org/10.1166/jnn.2019.16607>.
- [82] S. Booyens, M. Bowker, D.J. Willock, The adsorption and dissociation of CO on Fe(111), *Surf. Sci.* 625 (2014) 69–83, <https://doi.org/10.1016/j.susc.2014.02.019>.
- [83] G. T. Kasun Kalhara Gunasooriya, Mark Saeys, CO adsorption on Pt(111): from isolated molecules to ordered high-coverage structures, *ACS Catal.* 8 (11) (2018) 10225–10233, <https://doi.org/10.1021/acscatal.8b0237110.1021/acscatal.8b02371.s001>.
- [84] H. Jónsson, G. Mills, K.W. Jacobsen, Nudged elastic band method for finding minimum energy paths of transitions (1998) 385–404, doi:10.1142/9789812839664_0016.
- [85] G. Henkelman, B.P. Uberuaga, H. Jónsson, Climbing image nudged elastic band method for finding saddle points and minimum energy paths, *J. Chem. Phys.* 113 (2000) 9901–9904, <https://doi.org/10.1063/1.1329672>.
- [86] Graeme Henkelman, Hannes Jónsson, Improved tangent estimate in the nudged elastic band method for finding minimum energy paths and saddle points, *J. Chem. Phys.* 113 (22) (2000) 9978–9985, <https://doi.org/10.1063/1.1323224>.
- [87] R.A. Olsen, G.J. Kroes, E.J. Baerends, Atomic and molecular hydrogen interacting with Pt(111), *J. Chem. Phys.* 111 (1999) 11155–11163, <https://doi.org/10.1063/1.480473>.